# Dynamic Interplays between Phase Transformation Instabilities and Spatiotemporal Reaction Heterogeneities in Particulate Intercalation Electrodes

*Shubham Agrawal*[1] *and Peng Bai*[1,2,]*

[1]Department of Energy, Environmental & Chemical Engineering, Washington University in St. Louis, St. Louis, Missouri – 63130, United States

[2]Institue of Materials Science and Engineering, Washington University in St. Louis, St. Louis, Missouri – 63130, United States

*Email: pbai@wustl.edu

## Summary

Lithium-ion batteries rely on particulate porous electrodes to realize high performance, especially the fast-charging capability. To minimize the particle-wise reaction heterogeneities that may lead to local hot spots, deeper understandings of these electrodes at the mesoscale, i.e. hundreds of particles, have become an urgent need. This study reveals that the seemingly random reaction heterogeneities are actually controlled by the interplays between the non-equilibrium material thermodynamics and the electrochemical kinetics. Our *operando* experiments revealed that, during constant-current operations, there exist autonomous dynamic loops that control the intra- and inter-particle phase transformation dynamics that determine the true local current density. The combined theoretical and experimental analyses reveal that unlike other phase-transforming porous electrodes, not all phase separation processes in graphite electrodes can be suppressed by high currents. Our results highlight the necessity to examine the concentration-dependent exchange current density for intercalation electrodes undergoing complex phase transformation processes. Incorporating nonequilibrium thermodynamics into classical electrochemical models and electroanalytical techniques will ensure self-consistent understandings of practical porous electrodes toward precision design and management.


## Context and Scale

Amidst the quest towards ultrafast-charging lithium-ion batteries, the random occurrences of the accidents have increased. These accidents likely originate from the microscopic heterogeneities in the widely used phase-transforming electrode materials, e.g., graphite as a typical anode material. The degree of these reaction heterogeneities depends on the nature of phase transformation, either phase-separation or solid-solution. While the common consensus, based on $LiFePO_4$, suggests that phase-separations can be suppressed during fast ion intercalation, they have yet to be thoroughly validated for other electrodes. Understanding the origin and dynamics of reaction heterogeneities offers an important consideration in the design of the electrodes for their improved performance.

# 1. Introduction

The great success of lithium-ion batteries (LIBs) has allowed them to penetrate the markets of consumer electronics and electric vehicles.[1–3] The dynamic performance, cycle life, and safety of LIBs are directly dependent on the microscopic heterogeneities arisen from multiple fully-coupled electrochemical dynamic processes, which however are still not completely understood.[4,5] The state-of-charge (SOC) heterogeneities or non-uniform distribution of charge in both the phase-transforming[6–9] and solid solution[10–14] materials occur due to either the far-from-equilibrium thermodynamics of the active material or the heterogeneous microstructure of the composite electrode. In solid-solution cathode materials, in particular,[11,12,15] SOC heterogeneities were commonly attributed to structural heterogeneities, such as the non-uniform distributions of conductive additives, electrolyte, etc., but the actual root cause is worth careful examination, as the well-known solid-solution materials may exhibit "fictitious phase transformation" only under dynamic conditions that require *operando* characterizations.[16] The SOC heterogeneities in battery electrodes influence the accurate estimation of battery SOC in the battery management systems (BMS) which are responsible for their safe and reliable operation, prevention of physical damages, and handling of thermal degradation and cell unbalancing.[17–19] Sophisticated *operando* techniques employing synchrotron-based X-ray,[11,13,15,20–24] lasers[12,14] and visible light,[6,25–28] have been developed to generate valuable insights and obtain quantitative understandings about the effect of reaction heterogeneities on the intercalation mechanism and degradation behavior in the battery materials. Among them, the *operando* characterization using economical benchtop optical microscopes have demonstrated a well-rounded balance of large field of view with hundreds of particles, sub-micron resolution, fast imaging rate, and accurate interpretation of the electrochemical response.[12,14,25,27,28]

Graphite is one of the most studied carbon materials and is the dominant anode material for lithium-ion batteries, yet can be used as cathode in other battery systems.[29–32] Unlike other reversible electrode materials, graphite experiences multiple phase transformation steps upon ion intercalations, also known as ordered stages.[33–35] During lithiation into graphite, the optical characterization of phase transformation

reveals three major stages visible as blue (Stage 3), red (Stage 2), and gold (Stage 1) colors.[28,36] However, the widely accepted theory that the phase transformations can be suppressed[37] has not been rigorously tested in graphite,[36,38] due to the lack of cohesive combination of *operando* characterization tools and mathematical analyses. The complex phase transformation mechanisms in graphite affect its rate capability and cycle life and need a careful inspection to ensure improved performance.

Here, we use our benchtop *operando* platform to observe the reaction pathway of graphite (de)lithiation in real-time under both slow and fast galvanostatic conditions. Despite the 10 times difference in the applied total currents, direct image analyses revealed that the true local current densities are very similar. The phase transform dynamics appear to modulate both the numbers of reacting particles in the electrode and the propagation of phase boundaries in individual particles autonomously to achieve the most "comfortable" local current density for the composing particles. Our linear stability analysis based on the non-equilibrium thermodynamics provides the predictive explanations to the suppression or persistence of phase separation in these graphite particles. With the confirmation from phase-field simulations of 200 particles, the insights obtained from this study not only complement other advanced *operando* characterizations including those based on synchrotron X-ray, but also can help understand the effects of operation protocols of battery charging and discharging to minimize the dynamic heterogeneities toward longer battery cycle life.

## 2. Results

Our simple optical method has demonstrated the capability to reveal the subtleties of $Li^+$ ion (de)intercalation into practical graphite electrode under constant-voltage conditions, allowing the development of the boundary-length evolution kinetic model to understand the local electrochemical kinetics.[28] Here, under the practical constant-current conditions, the seemingly random phase transformation dynamics is found to be governed by the interplay between the non-equilibrium thermodynamics of the material and the true local current densities.

## 2.1. Phase transformations in galvanostatic cycling

We first evaluated the transition of colors in graphite particles (**Table S3**) from grey (Empty) to blue (Stage 3), to red (Stage 2) and to gold (Stage 1), under slow (0.1 C) and fast (1 C) galvanostatic conditions between 0.0004 V and 1.5 V vs $Li/Li^+$ in Li-graphite half cells (**Figure 1 and Video S1-S4**). The applied currents of 0.1 C and 1 C correspond to 0.034 $mA.cm^{-2}$ and 0.34 $mA.cm^{-2}$, respectively, based on the geometric area of the electrode. At the critical SOCs shown in Fig. 1 (a), all particles in the porous electrode appeared the same color, indicating the same stage, but the dynamic phase transformation processes between the critical stages were highly heterogeneous. The entire lithiation process followed a sequential phase transformation from empty to stage 3 (grey to blue, Step I), stage 3 to stage 2 (blue to red, Step II), and stage 2 to stage 1 (red to gold, Step III), which was reversed during delithiation. An accurate identification of the three stages via their respective colors in all the captured snapshots on the electrode-scale, serves as the backbone of the data analysis presented in this study. The consistency between net electrode capacity calculated from the image analysis (**See Experimental Section**) and the electrochemical measurements in **Figure S4**, confirms the accuracy of the image analysis. Hence, the evolution of the stable phases (**Figure S3**) and the length of the phase boundaries (**Figure S5**) in the entire electrode were estimated from the image analysis during the galvanostatic experiments. The initial grey to blue transition always follows a solid-solution reaction pathway, during which all particles react concurrently. To examine the intricacies of the two phase-transformation steps (II and III) closely, we selected five representative particles, P1 – P5, highlighted in **Figure 1A** and magnified in **Figure 1B – D**. We chose these five particles P1 – P5 randomly from the entire field of view based on their different shapes and sizes, as marked on the particle size distribution curve (**Figure S14**) obtained using ImageJ from the view under optical microscope. Such a selection would exclude any bias introduced while comparison particle-level phenomenon to the electrode-level phenomenon.

During 0.1 C lithiation (**Video S1**), the new phases in both phase transformation steps always nucleate at the particle edge to create sharp phase boundaries, which sweep across the particle to complete the phase

transformation. However, at a large scale, the intra-particle blue-red transformation is associated with a highly random and selective inter-particle dynamics (**Video S5**). Like the particle-by-particle intercalation in $LiFePO_4$ electrode at a low current,[20] the red phase nucleated in particle P3 first, followed by P1. Particles P2, P4, and P5 remained idle (blue) until P3 and P1 became completely red (**Figure 1B**). Moments later, the red phase nucleated in particle P2 and took nearly an hour to complete the transformation, whereas the smaller particles P4 and P5 easily transformed into red color, successively, due to smaller volume. A similar sequential blue-red transformation occurred in all the other particles, suggesting that only a limited fraction of the electrode was "active" at any instant. The red-to-gold phase transformation at 0.1 C current, however, started simultaneously in most of the particles (**Video S5**), within which sharp phase boundaries between the red (Stage 2) and gold (Stage 1) colors were still clearly visible. More obvious than in the blue-to-red transformation, smaller particles such as P4 and P5 incubated successful nucleations much sooner and got fully-filled much earlier than larger particles. The delithiation process at 0.1 C current triggered the random nucleations of the red phase (Stage 2) in most gold particles, essentially reversed the lithiation process until SOC reaches 55%, as shown in **Figure 1C** and **Video S2**. The red-to-blue (Stage 2 to 3) phase transformation reflected by the particles in the **Video S6** and last four columns of **Figure 1C**, however, did not follow the reversed pathway of particle-by-particle lithiation. Instead, it behaved more like the gold-to-red (Stage 1 to 2) transformation with most particles experiencing the phase transformation concurrently. Despite the subtle differences, it is evident that the phase transformations in Steps II and III occur through clear phase separation at slow galvanostatic condition during both lithiation and delithiation.

During the lithiation at 1 C current, the blue-to-red (Stage 3 to 2) transformation appeared more homogeneous than in the case of 0.1 C current, showing smeared phase boundaries and cloudy domains and thus, resembling a solid-solution mechanism, as visible in **Videos S3 and S5** and 22% - 39% SOCs in **Figure 1D**. This observation is consistent with the suppression of phase separation predicted[37] and confirmed[20,39] in $LiFePO_4$ electrodes. However, the red-to-gold (Stage 2 to 1) transformation remained unaffected by the elevated current density, random nucleations of the gold phase (Stage 1) at the edges of

multiple particles generated sharp phase boundaries that swept across the particles to complete the phase transformation, just like what we observed at 0.1 C current. The high reaction overpotential at 1 C current, shown in **Figure S1**, resulted in only 65% of the total capacity at the cut-off voltage, leaving a few particles partially lithiated, still with clear red-gold phase boundaries. These active phase boundaries within partially lithiated particles, visible in **Video S4**, may recede to disappear via inter-particle exchanges during a long time relaxation.[39] In our experiments, they started to move with newly nucleated phase boundary during the subsequent delithiation at 1C current, until all particles turned red (Stage 2). Unlike the rather homogeneous blue-to-red (Stage 3 to 2) lithiation at 1 C current, the red-to-blue (Stage 2 to 3) delithiation process at 1C always induced random nucleations and two-phase coexistence, as can be seen in the last four columns of **Figure 1D** and **Video S6**.

The above features of phase transformation in individual particles may differ from cycle to cycle. Since the graphite particles expand and contract repeatedly upon Li ion intercalation and deintercalation, the surface imperfections may slightly change and alter the surface energy. Thus, the nucleation of the stable phases could start at different spots on the particle edges in different cycles and the phase boundaries may evolve slightly differently. In addition, the nucleation in single particle may be influenced by the particle curvature as it affects the surface energy and may lead to easier nucleation due to surface wetting.[37,40] However, we focus on the less investigated spatiotemporal heterogeneities on the mesoscale and their impact on the local phase transformation dynamics. Despite these changes across different cycles, the charge and flux balances and the phase transformation mechanisms would remain same due to the inherent thermodynamics as discussed in the later sections.

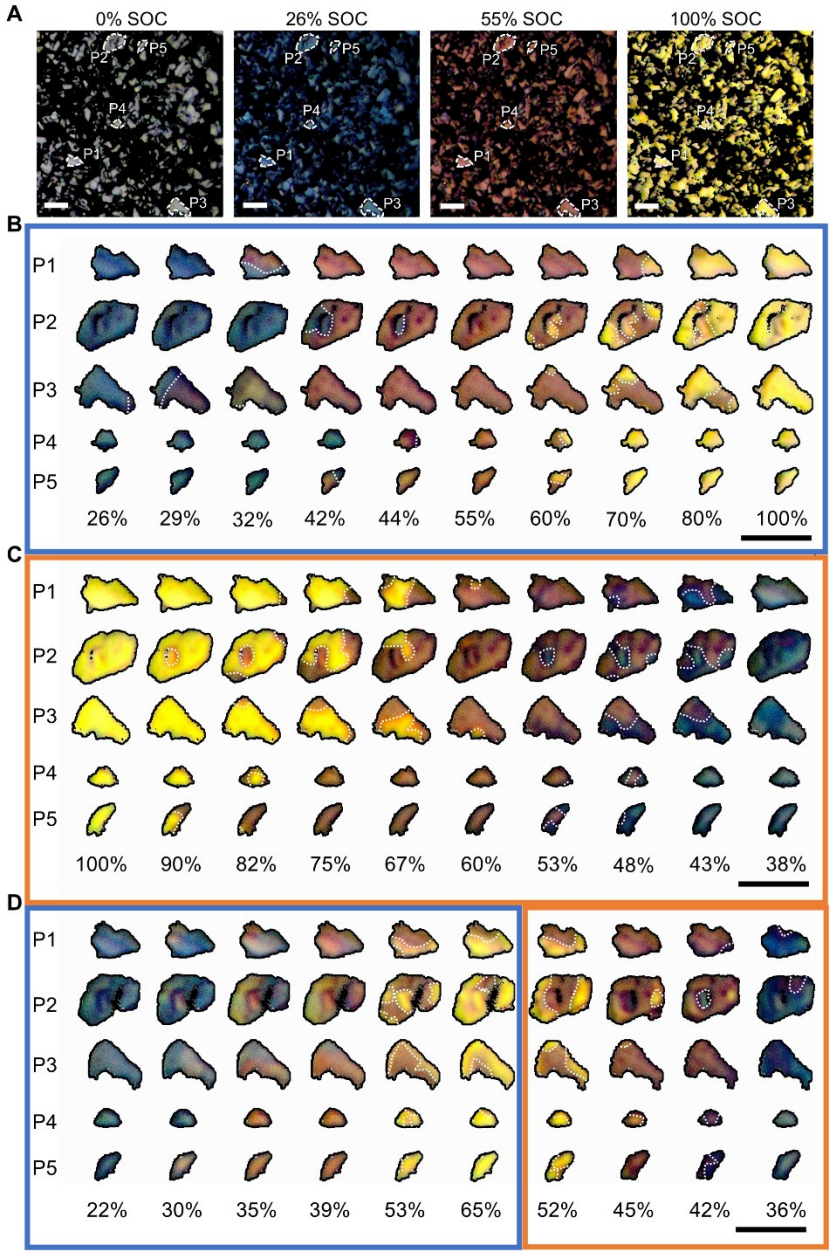


**Figure 1: Phase-transformation during (de)lithiation in graphite particles under constant current.** (A) The entire view of graphite electrode under the optical microscope in the empty state (grey), and stages 3 (blue), 2 (red), and 1 (gold). These frames are obtained at very low current (C/72) and are used as the calibration frames for the estimation of the SOCs of each stable phase. The white dashed outlines in these snapshots are the five selected particles (P1 – P5) for intra-particle inspection. (B) Lithiation process of the selected five particles at 0.1 C current. (C) Delithiation of the selected five particles at 0.1 C current. (D) Lithiation and delithiation of the selected five particles at 1 C current. The blue rectangle indicates lithiation while the orange rectangle denotes delithiation. The white dotted lines in the panels (B – D) indicate the phase boundaries generated during the phase transformations. The lithiation and delithiation processes at 0.1 C current show the phase transformations along the generated phase boundaries while the lithiation process at 1 C from 22% - 39% SOCs shows smeared phase boundaries and cloudy domains, resembling a solid solution mechanism. *Scale bar: 10 µm.*

The above observation raises two intriguing questions: (i) Why does the highly reversible graphite electrode show asymmetrical dynamics of phase transformation during lithiation and delithiation? (ii) Why the high current can suppress the phase separation in the blue-to-red transformation, but not the red-to-gold transformation?

## 2.2. True local electrochemical driving force

The surprising high resolution of the distinct colors in micron-sized particles allows determination of the local SOC by converting the color to the standard capacity associated with the color (stage). The calibration method of our analysis is explained in **Experimental Section** and **Figure S4**. Following the same principle validated at the larger scale, we further calculated the capacity evolution curves within the selected particles P1 – P5, as shown in **Figure S5**. In the solid-solution regimes, the capacities increased/decreased linearly in each particle, yielding low constant currents. However, in the phase-separation regimes, the total capacity within a particle was the net capacity contributed by each color. The total capacity remained constant when the particle was idling. We obtained the temporal variation of the current carried by each particle by taking the numerical first-order time-derivative of the capacity evolution curves, shown in **Figure S5**. These local "working" currents represent the true electrochemical conditions experienced by each particle, under the global slow and fast galvanostatic conditions.

To determine the local working *current density* for consistent transport analysis in each particle, the active reaction interfaces need to be identified in addition to the current. In general, $Li^+$ ions intercalate through all edge planes of the graphite particle and not the basal planes, as shown in the schematic in **Figure S17(a)**. The active reaction area is the product of the length of the perimeter and the thickness of the particle. This is true for the cases of the solid-solution pathway. However, in the cases of phase separation, almost all $Li^+$ ions quickly equilibrate within the stable phase domains and only make concentration jumps at the phase boundary between the two phases (colors), which is confirmed by the *operando* observations that the net $Li^+$ ion flux through the edges concentrates at the phase boundaries without causing any color change in the stable domains. In another word, $Li^+$ ion reaction flux at the particle edges is equivalent to the internal

$Li^+$ ion flux at the phase boundary that makes the phase boundary move. If the internal phase boundary does not move, no net electrochemical current will be seen on the edges of the particles. For consistent transport analysis, the flux that is normal to the particle edge but tangent to the phase boundary is less responsible for the movement of the phase boundary. Therefore, only the edges that are nearly parallel to the internal phase boundary should be counted as the effective reaction interface. We calculated the local working current densities or the interfacial current densities within each selected particle by dividing the local current with the associated active area, either the entire edge area for the solid-solution cases, or the phase boundary area for the phase-separation cases, as shown in **Figure 2A – D**.

As shown by the schematic highlight in **Figure 2E**, the single-particle level solid-solution behavior tends to induce concurrent reactions of all particles at the many-particle level. On the other hand, the single-particle level two-phase dynamics tends to activate just a few particles at a time[41,42], resulting in sequential reactions, which in turn yield a very high local working current density that can enable a solid-solution dynamics at the single-particle level. It is then not unexpected to discover that the true local current densities during phase separation are much higher than those in the solid-solution step (Figures 2A – D). More specifically, nucleation events of a new phase that led to the emergence of phase boundaries always caused sudden current density spikes. The positions of these spikes during lithiation at 0.1 C current in **Figure 2A** correspond to the particle-by-particle activation process. During the red-to-gold (Stage 2 to 1) lithiation at 0.1 C current, more active phase-separating particles lowered the absolute current shared by each particle and therefore lowered the true local current densities ($0.1 – 0.2\ mA\ cm^{-2}$) in individual particles shown in **Figure 2A**. The overlapping current densities are consistent with the relatively concurrent reaction among particles. During delithiation at 0.1C current, the obtained true local current densities are similar to those during the lithiation, only that the SOC ranges changed due to hysteresis between lithiation and delithiation.[43,44] In the case of 1 C current in **Figures 2C**, the solid-solution-like blue-to-red (Stage 3 to 2) lithiation makes the quantification of phase boundary improbable. Only the red-to-gold (Stage 2 to 1) lithiation exhibit phase-boundary-based high local current densities. True local current densities for the

delithiation process consistently reflect the existence of phase boundaries and the sequential reaction process.

It is evident from the above observations that, while the solid-solution mechanism led to a homogeneous distribution of the external driving conditions on the entire domain, the phase-separation caused higher working current densities on a limited number of reacting particles. These findings are consistent with the widely recognized theory that the nucleation a new phase via phase separation requires higher driving force than solid solution in the intercalation materials.[40,45] These interfacial current densities were 2-3 orders of magnitude higher than the average current density calculated using the BET surface area ($9.424\ m^2\ g^{-1}$). Surprisingly, a ten-fold increase in the external total current from 0.1 C to 1 C increased the actual working current densities by only up to five times. The high working current densities in the studied cases of phase transformation suggest a far-from-equilibrium (de)intercalation dynamics at both slow and fast galvanostatic conditions. These understandings also indicate that the process is not diffusion-limited,[28] and requires innovative theoretical analyses to uncover the underlying mechanisms.

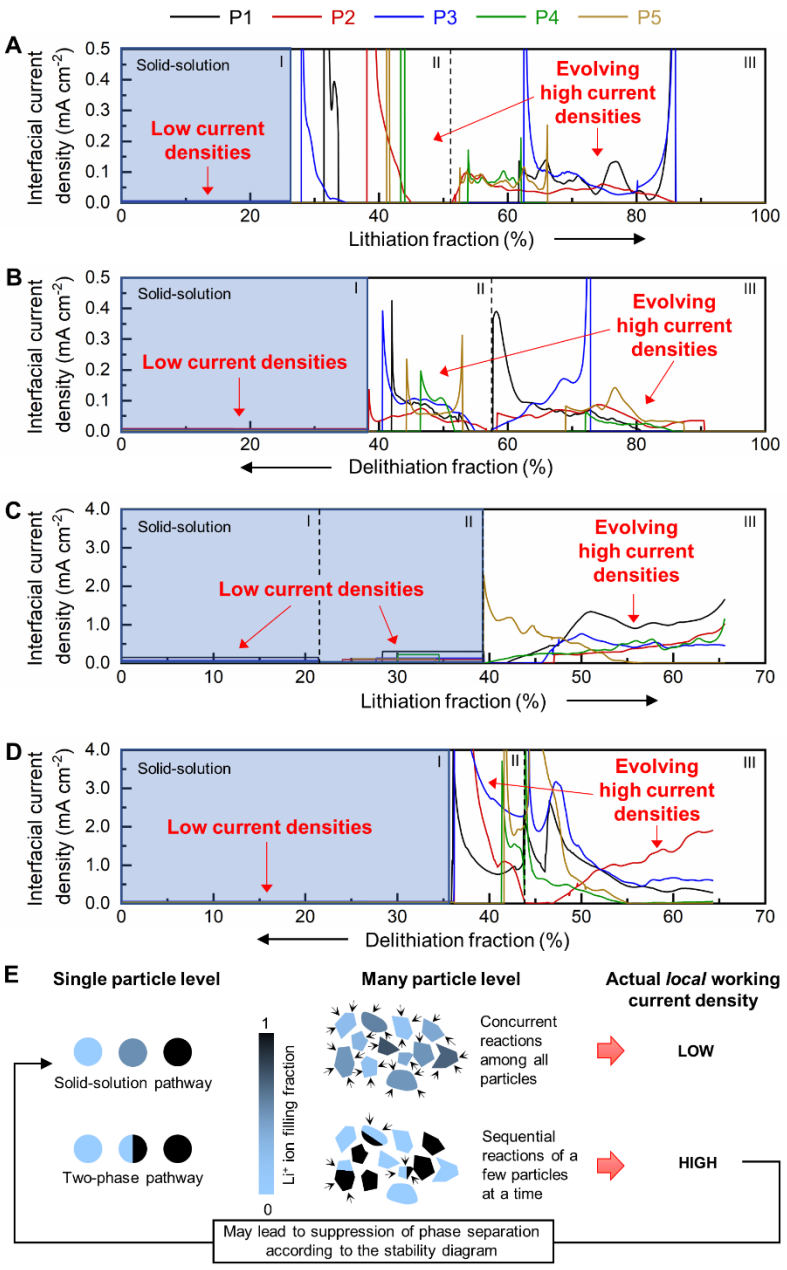


**Figure 2: Local working interfacial current densities during (de)lithiation in graphite under constant currents.** (A) Lithiation at 0.1 C current, (B) delithiation at 0.1 C current, (C) lithiation at 1 C current, and (D) delithiation at 1 C current. The solid-solution regions in these four panels (shaded in light blue in Step I and with the additional Step II for panel C) yielded low *local* interfacial current densities, while the two-phase regions yielded evolving but high local current densities. The distinct positions of the sharp peaks in Step II during lithiation at 0.1 C current indicate a particle-by-particle mechanism. The almost overlapping current density regions in the remaining phase-separation regimes show that the phase boundaries emerge simultaneously within these particles. (E) Schematic comparison of solid-solution pathway vs two-phase pathway at the single-particle level and many-particle levels, yielding different actual local current densities due to population of active particles[41] that in turn influence the single-particle dynamics.

## 2.3. Non-equilibrium thermodynamics of graphite

The thermodynamic origin of the electrochemical phase transformation has been well explained by the balance between the non-monotonic diffusional chemical potential and the applied electrochemical overpotential,[37,46] based on which it was predicted and verified in $LiFePO_4$ single particles[44] that phase separation, therefore the coexistence of two stable phases, can be suppressed by an external electrochemical driving force. Graphite, as another well-known phase separating material, has not been examined rigorously over the possibility of suppression of phase separation, despite a few attempts to explain the evolution of phase separation.[34,47,48]

Here, we performed a linear stability analysis[37] of the electrochemical phase transformation in a single graphite particle, by evaluating the dynamics of a linear perturbation, superimposed over a reaction-limited homogeneous system, but under various constant-current working conditions. An experimentally verified bilayer regular solution model[33,49] (not to be confused by the electrical double layer in a liquid solution) was adopted here to investigate the stabilities. The bilayer regular solution model allows the filling fraction $\tilde{c_1}$ to vary between 0 and 1 while $\tilde{c_2} \sim 0$ for blue-red (Stage 3 to 2) phase transformation; once $\tilde{c_1} \sim 1$, the second filling fraction $\tilde{c_2}$ starts to increase during red-gold (Stage 2 to 1) phase transformation. As presented in **Supplemental Information Section 7**, our theoretical analysis provides the normalized growth speed of the perturbation with wave number k for the blue-red transformation,

$$\tilde{s_1}(\tilde{k}, \tilde{c_1}, \tilde{J}) = \left[2\tilde{\Omega}_a + 2\tilde{\Omega}_c\tilde{c_2}(1-\tilde{c_2}) - \frac{1}{\tilde{c_1}(1-\tilde{c_1})} - \tilde{K}\tilde{k}^2\right]\sqrt{\frac{\tilde{J}^2}{4} + [F(\tilde{c_1})]^2} + \left(\frac{F'(\tilde{c_1})}{F(\tilde{c_1})} + \frac{1}{2}\tilde{K}\tilde{k}^2\right)\tilde{J} \quad (1)$$

where $\tilde{\Omega}_a$ and $\tilde{\Omega}_c$ represents the regular solution coefficients for the intra-layer and inter-layer particle-vacancy interactions respectively; $\tilde{K} = V_S K/k_B T L^2$ is the dimensionless gradient penalty parameter dependent on the volume per intercalation site $V_S$, diffusion length $L$, Boltzmann constant $k_B$, and the room temperature $T$ taken as 298 K. Following a similar strategy, the stability equation of the growth speed during red-gold phase transformation is slightly different,

$$\tilde{s_2}(\tilde{k},\tilde{c_2},\tilde{J}) = \left[2\tilde{\Omega}_a + 2\tilde{\Omega}_c\tilde{c_1}(1-\tilde{c_1}) - \frac{1}{\tilde{c_2}(1-\tilde{c_2})} - \tilde{\mathrm{K}}\tilde{k}^2\right]\sqrt{\frac{\tilde{J}^2}{4}+1} + \left(\frac{1}{2}\tilde{\mathrm{K}}\tilde{k}^2\right)\tilde{J} \qquad (2)$$

Apparently, the growth speeds $s_1$ and $s_2$ depend on $\tilde{J}$, which is the local interfacial current density $J$ scaled to the concentration-dependent exchange current density in the homogeneous state $J_0(\tilde{c_i}) = k_0F(\tilde{c_i})$ with $k_0$ being the rate constant and $F(\tilde{c_i})$ being the normalized exchange current density function for respective phase transformations. The complete derivation of Equations (1) and (2) can be found in **Supplemental Information, Section S7**. It is important to note that the local exchange current density is an intrinsic interfacial property and needs to be determined experimentally in a self-consistent manner using the area of the active sites, instead of the total or apparent area. Based on our *operando* observations, image analyses, and impedance diagnosis,[28] the intrinsic exchange current densities for particles in the solid-solution and red-gold (Stage 2 to 1) phase transformation states are relatively independent of the $Li^+$ ion filling fraction as *0.5 mA cm*$^{-2}$ and *3 mA cm*$^{-2}$. The exchange current density for particles in the blue-red (Stage 3 to 2) phase transformation, however, is sensitive to the filling fraction and appears as a skewed non-monotonic curve in **Figure S8**.

With the consistent exchange current densities and the regular solution coefficients, we plotted in **Figure 3** the neutral and driven linear stability boundaries, $\tilde{s}_{max}(\tilde{k},\tilde{c_1},\tilde{J}) = 0$ and $\tilde{s}_{max}(2\pi,\tilde{c_1},\tilde{J}) = |\tilde{J}|$, using the most unstable mode $\tilde{k} = 2\pi$. The regular solution coefficients govern the nucleation barrier of the respective phase transformations. The shape of the stability boundaries is thus dictated by both the regular solution coefficients and the exchange current densities due to their ability to affect the growth speeds, as shown in Equations (1) and (2). The stability boundary for the blue-red (Stage 3 to 2) phase transformation in Figure 3A has a maximum, resembling the diagram for $LiFePO_4$.[37,44] The relatively constant exchange current density for the red-gold (Stage 2 to 1) phase transformation, however, leads to different stability boundaries that do not close to reaching a maximum, as shown in Figure 3B.

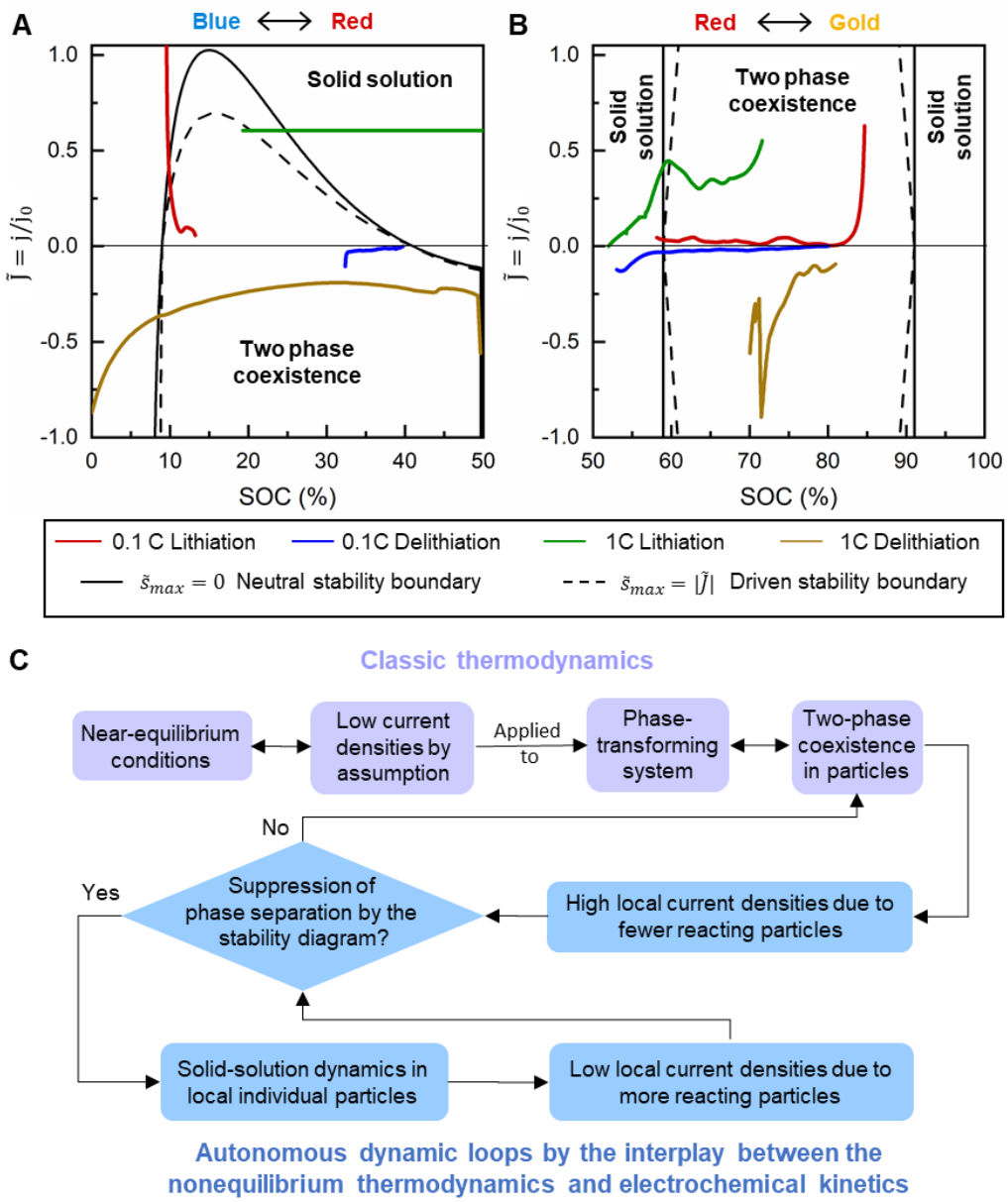


**Figure 3: Comparison of *operando* current densities and the linear stability diagram for graphite single particles.** Linear stability diagram for (A) blue to red (Stage 3 to 2), and (B) red to gold (Stage 2 to 1) phase transformations during both lithiation and delithiation at both the galvanostatic conditions. The experimental *operando* current densities (Steps II and III) lie within the domains of two-phase coexistence in all the cases except the blue-red (Stage 3 to 2) lithiation process at 1 C current (green solid curve in the SOC range of 20% to 50% in panel A). This observation is consistent with the visual examination of the (de)lithiation process shown in Figure 1. Current density data displayed here are from particle P1. (C) The dynamic interplay between the nonequilibrium thermodynamics and electrochemical kinetics reveals the autonomous dynamic loops regarding the intra- and inter-particle behaviors, as depicted in the flowchart.

The linear stability diagram acts as a "nonequilibrium electrochemical phase diagram" generated from the interplay between the nonequilibrium thermodynamics of the materials and the exchange current densities at the materials interface. The stability diagram is a rigorous quantitative summary of the dynamic interplay. As shown in the flowchart (Figure 3C), conventional understandings following the classic thermodynamics would consider that a near-equilibrium excitation will only induce near-equilibrium dynamics. Therefore, a low current applied to phase-transforming electrodes would induce two-phase coexistence in every single particle. However, as we proved here in complex phase-transforming electrodes like graphite, phase separation will lead to highly localized current density, that may lead to the suppression of phase separation and thereafter the solid-solution dynamics, but only if an SOC-dependent non-monotonic exchange current density is in place. As discussed above, the phase separation can then be suppressed only in the blue-red (Stage 3 to 2) phase transformation regime, owing to a skewed concentration-dependent exchange current density. Due to the non-monotonic stability curves for the blue-red (Stage 3 to 2) phase transformation during the lithiation process, there exist critical current density $\tilde{J}_{BR}^{c}$ ~ 1.02 beyond which the phase transformation would occur via the solid-solution pathway. On the other hand, the diverging unstable region for the red-gold (Stage 2 to 1) phase transformation during both the lithiation process and the delithiation process suggests that the respective phase separations will always be triggered, irrespective of the current densities. Take particle P1 as an example, we overlay the *operando* interfacial current densities from **Figure 2** on the stability diagram **Figure 3**, and observed that only the blue-red (Stage 3 to 2) transformation during lithiation at 1 C current lied close to the critical current density $\tilde{J}_{BR}^{c}$, where a dynamic solid-solution pathway becomes possible. The *operando* current densities during the other phase transformation processes, however, lied within the phase-separation domains for all the phase transformations. Similar results were obtained for the other four particles and are shown in **Figure S9**. It should be noted that the regular solution model spans across the entire SOC range from 0%, to 100% SOCs, while the actual phase-transformation in our electrodes occurs within different SOC ranges shown in **Table S1**. To better compare them, the *operando* interfacial current densities have been scaled (only horizontally along the SOC axis) to match the phase-transformation SOC ranges of the regular solution model. This

theoretical understanding offers a consistent explanation of the visually obtained local current densities during phase transformations and indicates that the dynamics is indeed controlled by the *operando* electrochemical flux, and not the solid-state diffusion.

## 2.4. Simulations of mesoscale many-particle dynamics

The single-particle analyses necessitate the incorporation of non-equilibrium materials thermodynamics into electrochemical models[37,46,50] toward the holistic design of battery materials and electrodes. Here, we adopt the multiphase porous electrode theory (MPET) developed by the Bazant group,[51] which not only incorporates materials thermodynamics for phase transformation, but also can predict the transport processes through the electrode that can also be modeled by the classic porous electrode theory pioneered by J. Newman.[52,53] With the consistent kinetic parameters, i.e., $Li^+$ ion diffusion coefficient $D_{Li}$ and exchange current density $j_0$, now extracted from our *operando* experiments, we modeled 200 thin flake-like square graphite particles to simulate the many-particle dynamics in practical surroundings. The cluster of particles has a fixed thickness ($0.5\ \mu m$) with both the length and width dimensions (same for square particles) lognormally distributed with a mean and standard deviation of $8.13\ \mu m$ and $2.61\ \mu m$, respectively (same as experiments). The model framework adopts a two-parameter Cahn-Hilliard reaction theory where the equilibrium voltage curve is represented by a periodic bi-layer regular solution model.[33] The regular solution model implicitly controls the nucleation barrier of individual phase transformation via the regular solution coefficients, as shown in Equation (S1). The reduced 1D simulation with surface reaction boundary condition applied on both ends of the particle was performed. Thus, the $Li^+$ ions can enter the graphite particles only from the two opposite ends, as schematically shown in **Figure S17(b)**. To replicate the true local dynamics, we employ the values of the $Li^+$ ion diffusion coefficient in graphite $D_{Li}$ ($9 \times 10^{-8}\ cm^2\ s^{-1}$) and the rate constant $k_0$ ($8.3\ mA\ cm^{-2}$) evaluated from the *operando* interfacial current densities in our recent work,[28] with the Cahn-Hilliard gradient penalty parameter $K$ required in the equilibrium voltage calculation as $5 \times 10^{-7}\ J/m$ for the phase transformations.[38] The details of the MPET model can be found in multiple

reports by Bazant and collaborators.[33,36,51,54] The key governing equations used in the model are presented in **Supplemental Information Section 9**.

As suggested in Section 2.2, we studied the phase transformation by evaluating the progression of the area fractions of the stable phases in the lognormally distributed particles. With the particle size sorted in ascending order and assigned respective numerical IDs as shown in **Figure 4**, we identified the phases based on the concentration gradient at the phase boundaries, similar to **Figure S10** for Particle ID #100. Here, the solid-solution processes, which include both the empty (grey) to Stage 3 (blue) and Stage 3 (blue) to Stage 2 (red) lithiation at 1C (but not at 0.1C), would appear blue. In cases of phase separation, the vertical line/region corresponding to each particle ID will show the coexistence of the two colors in accordance with the respective phases. The lithiation at 0.1 C current (**Figures 4A – D**) began with homogeneous intercalation within all particles until the battery voltage reaches the spinodal point (~4% SOC), which triggered the blue-red (Stage 3 to 2) transformation.[37] The smaller particles showed the blue-red phase boundaries first and became completely red before inducing the phase transformation in new particles. This particle-by-particle filling mechanism continued in the electrode without any appearance of the gold color, except in a small overlapping SOC range of 50% - 60%. Multiple particles activated during the red-gold (Stage 2 to 1) phase transformation and possessed phase boundaries simultaneously. But the smaller particles tend to completely transform into gold earlier than the larger ones. The lithiation at 1 C current (**Figures 4C – H**), however, mapped blue color in all the particles up to ~34% SOC, indicating that the blue-red (Stage 3 to 2) phase transformation continued the solid-solution behavior even after all the particles reached stage 3. While some smaller particles exhibited the blue-red phase boundaries, the gold (Stage 1) color appeared at ~37% SOC. The red-gold (Stage 2 to 1) phase transformation then continued similar to the lithiation at 0.1 C current with significant remaining phase boundaries at the end, due to a reduced electrode capacity at the cut-off voltage (~65%). The delithiation process at both 0.1 C and 1 C currents, however, exhibited gold-red (Stage 1 to 2) and red-blue (Stage 2 to 3) phase transformations via the respective phase boundaries, as shown in **Figure S11**. The model response was consistent with the

experimental *operando* observations, confirming its validity. The accurate prediction of the phase transformation pathways at both low and high currents provides a validation of the kinetic parameters and also demonstrates the predictive capability of MPET to understand the dynamics of the battery materials.

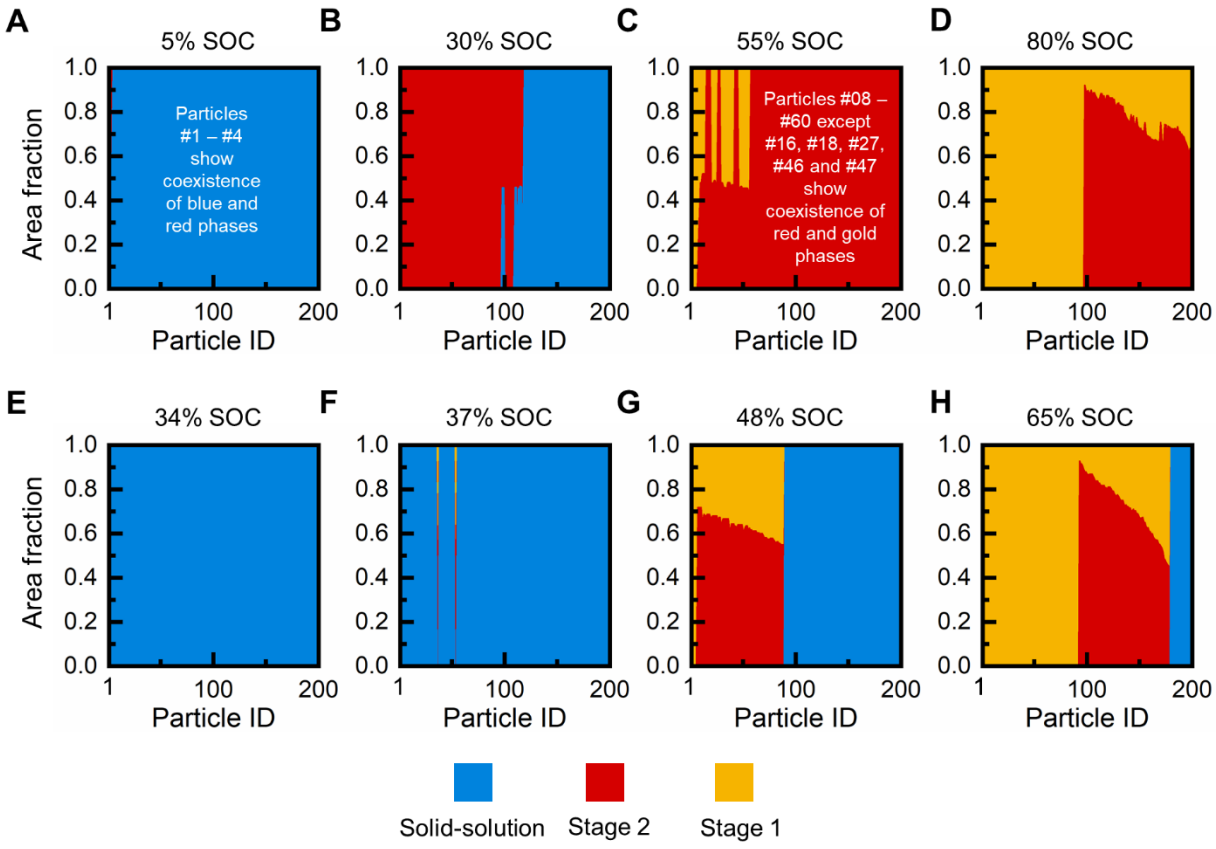


**Figure 4: Theoretical predictions of area fraction of the stable phases using MPET with 200 lognormally distributed particles.** Area fraction of stages 3, 2 and 1 at four global SOCs at (A – D) 0.1 C current, and (E – H) 1C current. The increasing particle IDs signify increasing particle lengths. At 0.1 C current, the blue-red phase boundaries appear initially in smaller particles. The new phase boundaries begin only when the phase transformation in the earlier particles is finished. On the other hand, the solid solution behavior continues up to ~34% at 1 C current which means that the blue-red (Stage 3 to 2) phase transformation also occurs almost via the solid-solution mechanism. Once almost all particles are in stage 2, the red-gold (Stage 2 to 1) transformation occurs along the phase boundaries at both currents.

In addition to the qualitative consistency, the simulations allow evaluation of the instantaneous total interface length within the simplified ideal rectangular particles, using the concentration gradient at the phase boundaries. Based on the 1D simulation, the phase boundaries emerged parallel to the active dimension of the particles. Thus, the total length of the phase boundaries was equal to the collective size of

the active particles and could be extrapolated to the total volume of the graphite electrode used in the experiments. These simulated spatiotemporal responses of phase boundaries in the considered galvanostatic conditions, during both lithiation and delithiation, despite notable deviations, were in the same orders of magnitude with the *operando* observations, as shown in **Figure 5A – B** and **Figure S12**, respectively. The widened curves and shifted peaks in the simulated lengths of the phase boundaries, as compared to the image analyses, are mainly due to the inconsistency introduced by the simple 1D particles, in which the ideal 1D phase boundaries cannot reflect the 2D results perfectly. While the numerical challenges in simulating hundreds of realistic 2D particles will be addressed in our future works, the comparison shown in Figure 5 is still deemed meaningful, as it closes the loop of our analysis: using kinetic parameters ($D_{Li}$ and $k_0$) extracted from true local electrochemical processes and incorporating nonequilibrium materials thermodynamics enable mathematical simulations that can capture the spatiotemporal heterogeneities at multiple scales in complex phase-transforming electrodes.

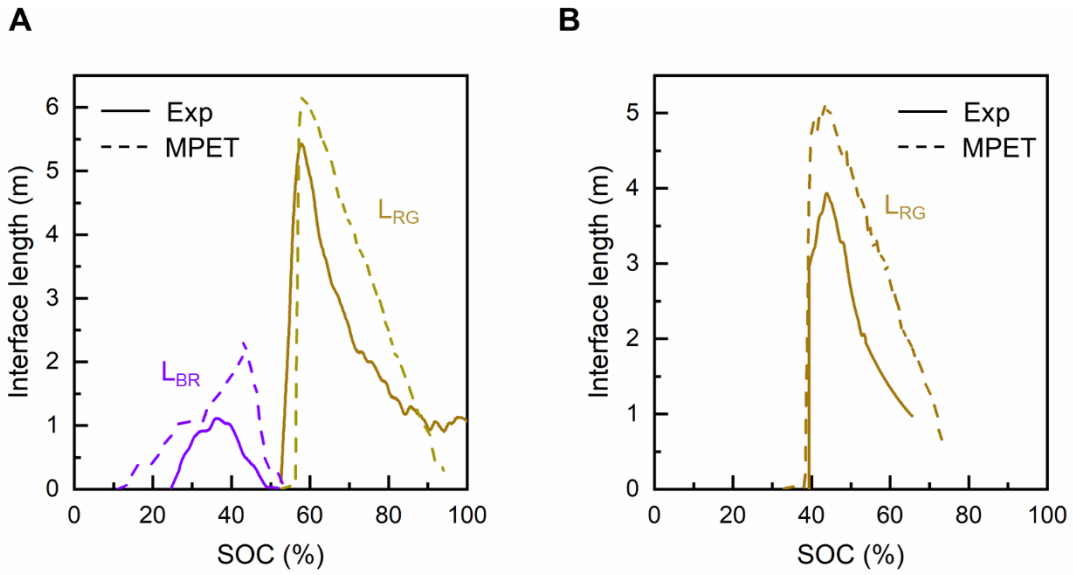


**Figure 5: Comparison between lengths of phase boundaries extracted from direct image analysis (solid lines) and that simulated using MPET (dashed lines) at (A) 0.1C current, and (B) 1C current.** The blue-red (Stage 3 to 2) transformation begins earlier in the simulation than in experiments because the simulation triggers phase-transformation when the $Li^+$ ion concentration reaches a spinodal point (~4% SOC) in the regular solution equilibrium voltage curve.

## 3. Discussion

Quantifications of the phase boundaries and hence the *operando* interfacial current densities provide a consistent understanding of the active reaction fronts and the local electrochemical activity in the phase-transforming porous electrodes. A three-orders-of-magnitude higher interfacial current density than the averaged one, at a low current of 0.1 C, suggests a far-from-equilibrium dynamics as opposed to widely known near-equilibrium process, and necessitates special attention in interpreting experimental data. Moreover, a comparable magnitude of interfacial current densities at 0.1 C and 1 C currents highlights that the local reaction flux remains almost unchanged on increasing the total current, as the interfacial reaction appears to be autonomously coordinated and modulated by the phase transformation dynamics among many particles. Despite the similar orders of magnitude of the interfacial current densities at low and high currents, the intercalation mechanism may be different, owing to the intrinsic exchange current density affected by the local filling fraction.[28] The electrochemical stability diagram (**Figure 3)** obtained from the linear stability analysis with the constant-current integral constraint shows that only the blue-red (Stage 3 to 2) phase transformation during the lithiation process can be suppressed at a high current, while red-gold (Stage 2 to 1) phase transformation would always occur via a two-phase coexistence, consistent with the visual observations. However, our *operando* experiments at 1.5 C and 2 C currents show that in real battery operation, the much larger overpotential resulted in the incomplete charge/discharge at the cut-off voltages, that the capacity obtained at such high currents would be insufficient to start the red-gold (Stage 2 to 1) transformation, as shown in **Figure S1**. Therefore, the spatiotemporal heterogeneities seem to dampen at high currents in our thin graphite electrodes shown in **Figure S13**.

There are two experimental aspects pertinent to this study, enabling the successful analysis of the spatiotemporal heterogeneities. Firstly, we ensured a low thickness of the electrode (~ 5 μm) to avoid the occurrence of the reaction heterogeneities in the thickness direction due to the concentration gradient in the electrolyte.[6,15,23] A consistent comparison between the total capacities obtained from the electrochemical experiments and the direct image analyses, confirms a similar level of reaction heterogeneities in the entire

electrode. Secondly, we used flake-type graphite particles to allow easy in-focus imaging of hundreds of particles with high resolution at the single-particle level. While the natural graphite flakes are susceptible to the stacking defects due to polycrystalline nature, the degree of defects depend on the size of the flakes.[55] The flakes with average size of 8 μm used in this study, have less stacking defects. Thus, the layers can be considered parallelly stacked and suitable for Li ion intercalation. The absence of such defects and crystalline domains within a particle is further justified by the nucleation of phases only at the particles' edges and not internally. Hence, the light color patches seldomly appearing in the low Li content images are probably due to the surface roughness of the particles and are accounted for using a range of Hue for each stable phase during image segmentation (**See Experimental Section and Figure Sxx**). These structural imperfections can also affect the direction of phase boundaries within the particles. The many-particle MPET simulation represents an ideal system with square-shaped single-domain particles. The 200 particles/domains in the MPET simulation are arranged parallelly with each other and can statistically represent the entire electrode. The conclusions, based on the fundamental material properties, apply to other types of graphite such as mesocarbon microbeads (MCMB) and synthetic graphite, in which phase transformation and reaction heterogeneities were already observed.[6,56]

A recent scaling analysis suggests that the $Li^+$ ion intercalation in large graphite particles of 50 μm[38] and 400 μm[57] is diffusion-controlled, but according to our latest observations,[28] the intercalation process in our graphite flakes (< 10 μm) at mesoscale is not diffusion-controlled, but rather governed by phase-transformation that determines both the number of reacting particles (therefore the true local current density) and the evolution of the phase boundaries in individual particles. For this reason, the classical electroanalytical methods developed under the assumption of diffusion-controlled scenario may not be used without careful examination to extract the kinetic parameters, i.e. $D_{Li}$ and $j_0$.[28,58,59] To fully understand the autonomous dynamic loops (Fig. 3C), it is necessary to incorporate electrochemical phase-field models for single particles with porous electrodes theories for the electrode, like the MPET model we used here. In this study, we considered lognormally distributed square-shaped particles with intercalation only along one

dimension. Although rectangular particles with fixed width and lognormally distributed length dimension would represent actual graphite particles more accurately, it may cause theoretical inconsistency in a 1D simulation. Our 1D simulation lacks the feature to choose the direction of intercalation based on surface energy which may contradict that the phase boundaries align preferentially towards the shorter dimension. Further improvements of the code, by using consistent particles shapes and performing 2D or 3D simulations, would enable more accurate agreement with the experimental true local current densities and the intra- and inter-particle dynamics.

Although the current study focuses on the intercalation mechanisms in flake-like graphite particles, the methodology can be translated to the other varieties of graphite due to the common phase transformation behavior. In graphite such mesocarbon microbeads[6] and synthetic graphite,[56] different surface energy can affect the nucleation barrier and the reaction sequence of the particles but they still show phase transformation dynamics and severe reaction heterogeneities. With accurate regular solution coefficients and exchange current densities, the stability diagram similar to Figure 3 can be obtained for other graphite types with the aid of proper image analysis, to evaluate the phase transformation dynamics.

## 4. Conclusion

We have utilized a simple benchtop *operando* setup to observe the spatiotemporal heterogeneities in practical graphite electrodes under various constant current densities. Unlike other well-known phase-transforming battery materials, not all phase separation processes in graphite can be suppressed by a high current. By comparing the true local current density of a single particle from direct image analysis with the linear stability diagram of electrochemical phase transformation, it is now clear that whether an ion-intercalation-induced phase transformation can be suppressed or not, depends on the dynamic interplay via the interfacial kinetics. An SOC-dependent (concentration-dependent) non-monotonic exchange current density is the premise for the suppression of phase separation, via the autoinhibitory pathway.[60] Beyond the consistent single particle analysis, a many-particle model was developed to understand the mesoscale behavior of the electrode, by using the MPET code. The results reveal a good agreement between the phase

boundaries identified from direct image analysis and from simulation, which valid our self-consistent close-loop analysis for more effective battery design strategies.

# 5. Experimental Section

**Thin electrode preparation:** We formed a homogeneous graphite slurry by dissolving graphite flakes (7-10 µm, 99%, Alfa-Aesar), PVdF binder (>99.5%, MTI Corp) and conductive acetylene black powder (35-40 nm, MTI Corp) in the ratio 88:10:2, in 1-methyl-2-pyrrolidone (NMP, 99.5%, Sigma Aldrich). This slurry was coated onto separator film by the doctor-blade method. We, then, dried the electrodes at 60°C to remove the NMP, punched out Φ8 mm electrodes and kept them under vacuum at 70°C for 12 hours to remove the residual moisture. The active material loading, and electrode thickness were 0.7 mg $cm^{-2}$ and 5 µm, respectively, shown in Figure S13.

***Operando* setup and experiments.** We assembled a graphite half-cell with a Li anode, a glass-fiber separator, and 1M $LiPF_6$ in EC:DMC (50:50 v/v) in a standard 2032 coin cell with a Φ2 mm hole on the top, in an Ar-filled glovebox. We sealed the viewing hole with a 5 x 5 mm glass window using epoxy to seal the cell to view the graphite flakes under the optical microscope Olympus BX53M microscope with objective 50x for *operando* observation. We ran five formation cycles at 0.25 C between cut-off voltages 1.5V and 0.4 mV. We then, performed a galvanostatic charge and discharge at 0.1 C and 1 C currents, and captured the frames every 20s and 2s time intervals, respectively. All the acquired digital photos were processed using ImageJ to quantify the colored regions. The detailed description of the procedures is mentioned below.

**Color thresholds for area quantification.** We used the built-in color threshold method of ImageJ identify the blue (Stage 3), red (Stage 2) and gold (Stage 1) colors based on the Hue, Saturation and Brightness in the frames captured in the *operando* galvanostatic experiments. The brightness difference of blue, red and gold colors caused some smaller particles (< 2 µm), which were not clearly visible when they were blue or red, to get illuminated upon turning into gold color. Since ImageJ auto-selects all the non-black regions/graphite flakes according to the brightness, this illumination resulted to select more area when the particles entered Step III (or Stage 1). The difference in the selected area across all the images was always under 10%, resulting in slight inconsistency while calculating the area fraction of different phases.

To avoid this inconsistency, the same sampling region was defined based on the images with all red-colored particles while converting the surrounding areas black. The black mask constituted all the non-particles regions and the unreacted regions obtained from 100% SOC image. This final black mask was applied to all the images. Within the sampling regions, a fixed range of hue was used to select similar colored regions (Red: 0 – 24, Gold: 24 – 44, and Blue: 44 – 255) while maintaining the same range of saturation and brightness. The above criteria were applied to all the digital images with the help of an ImageJ script. The conversion of three representative images is shown in Supplemental Information Figure S15. A variation of ±10% in the selected thresholds results in a deviation of only ±0% – 5% in the selected areas of blue, red and gold.

**Charge conservation calibration.** We first converted the blue, red, and gold colors into the standard RGB colors using our segmentation algorithm in ImageJ, explained above, and determined the evolution of area fractions ($a_i$) of these colors in the overall view (**Figure S3**). Since these colors represent stable phases of the lithiated graphite, they have a fixed SOC with respect to the total electrode capacity, associated with them. During phase transformation at near-equilibrium conditions, the transformed particles wait until the entire electrode reaches the same state, making the SOC of that particular state same as the global SOC. Hence, we determined the SOCs of the blue ($x_B$), red ($x_R$) and gold ($x_G$) colors as 26%, 55% and 100% under low galvanostatic conditions (C/72 current). We used these SOC values for the validation of our color segmentation algorithm with the electrochemical response, via charge conservation within the electrode, $\sum_i q_i A_i(t) = q_T(t) A_T$, where $i$ represents Blue, Red, and Gold, $q_i$ is the areal capacity of the $i^{th}$ color and can be calculated from the SOC of the $i^{th}$ color (estimated above) and the theoretical areal capacity of the material ($q_o$), $q_i = x_i q_o$, $A_i$ is the area covered by $i^{th}$ color, $q_T$ is the areal capacity of the electrode and $A_T$ is the total surface area of particles in the electrode. The above equation can, then be transformed into $\sum_i x_i a_i(t) = x_T(t)$ where $a_i$ is the area fraction of the $i^{th}$ color, and $x_T$ is the global SOC of the electrode. For known area fractions of stable phases, a phase-transforming material should inherently follow this equation. Since we only observed a 100 × 100μm window under the optical microscope, the validity of the

above equation for the observed region confirms that the analysis can be confidently extrapolated to the entire electrode (**Figure S4**).

**Determination of the effective interfacial area:** For a shape with two colors, we used ImageJ to find the perimeter covered by each color, and the outer perimeter of the shape, which together can be solved for the length of the interface. In our case, particles existed in three different states at a time. To calculate the length of the interface, for instance, the Blue – Red interface, we relied on the fact that the phase transformation in graphite can only occur in one order: Stage 3 to Stage 2 to Stage 1. We converted all the green regions in the transformed RGB images, to the standard red color, thus eliminating all Red – Gold interfaces. This enabled us to find the length of the Blue – Red interface using the above methodology from the following equation, $L_{BR} = (l_{Blue} + l_{Red} - l_{particles})/2$. Similarly, we calculated the length of the Red – Gold interface by converting all the blue regions to the standard red and applying following equation, $L_{RG} = (l_{Red} + l_{Gold} - l_{particles})/2$ where $L_{BR}$ and $L_{RG}$ are the lengths of Blue – Red and Red – Gold interfaces respectively, $l_{Blue}$, $l_{Red}$ and $l_{Gold}$ are the perimeters of the blue, red and gold regions in the corresponding transformed images, and $l_{particles}$ is the outer perimeter of all the particles within the viewing frame. The representative image conversion to calculate the interface lengths in particle P1 is shown in Figure S16.

Considering disc-shaped flakes with an average diameter 8µm and thickness 0.5 µm, our ~5 µm thick electrode constituted ~$10^7$ particles with 10 layers stacked over each other. On making a statistical assumption that all layers were similar, we calculated the active area by multiplying the total length of phase boundaries with the electrode thickness.

**Acknowledgment**

P.B. acknowledges the support from a National Science Foundation grant (Award No. 2044932) and the faculty startup support from Washington University in St. Louis. The materials characterization experiments were partially supported by IMSE (Institute of Materials Science and Engineering) at Washington University in Saint Louis.

**Author contributions**

P.B. conceived and supervised the study. S.A. and P.B. designed the experiments. S.A. performed the experiments, carried out the analysis. S.A and P.B. wrote and revised the manuscript.

**Additional information**

Supplemental information is available online.

**Competing interests**

The authors declare no competing financial interests.

**Data availability**

The data that support the findings of this study are available from the corresponding author upon reasonable request.

# References


1. Tarascon, J.M., and Armand, M. (2001). Issues and challenges facing rechargeable lithium batteries. Nature *414*, 359–367.

2. Choi, J.W., and Aurbach, D. (2016). Promise and reality of post-lithium-ion batteries with high energy densities. Nat. Rev. Mater. *1*.

3. Goodenough, J.B., and Kim, Y. (2010). Challenges for rechargeable Li batteries. Chem. Mater. *22*, 587–603.

4. De Jesus, L.R., Zhao, Y., Horrocks, G.A., Andrews, J.L., Stein, P., Xu, B.X., and Banerjee, S. (2017). Lithiation across interconnected V2O5 nanoparticle networks. J. Mater. Chem. A *5*, 20141–20152.

5. Massé, R.C., Liu, C., Li, Y., Mai, L., and Cao, G. (2017). Energy storage through intercalation reactions: Electrodes for rechargeable batteries. Natl. Sci. Rev. *4*, 26–53.

6. Harris, S.J., Timmons, A., Baker, D.R., and Monroe, C. (2010). Direct in situ measurements of Li transport in Li-ion battery negative electrodes. Chem. Phys. Lett. *485*, 265–274.

7. Liu, J., Kunz, M., Chen, K., Tamura, N., and Richardson, T.J. (2010). Visualization of charge distribution in a lithium battery electrode. J. Phys. Chem. Lett. *1*, 2120–2123.

8. Qi, Y., and Harris, S.J. (2010). In situ observation of strains during lithiation of a graphite electrode. J. Electrochem. Soc. *157*, 741–747.

9. Chueh, W.C., El Gabaly, F., Sugar, J.D., Bartelt, N.C., McDaniel, A.H., Fenton, K.R., Zavadil, K.R., Tyliszczak, T., Lai, W., and McCarty, K.F. (2013). Intercalation pathway in many-particle LiFePO4 electrode revealed by nanoscale state-of-charge mapping. Nano Lett. *13*, 866–872.

10. Tian, C., Xu, Y., Nordlund, D., Lin, F., Liu, J., Sun, Z., Liu, Y., and Doeff, M. (2018). Charge

Heterogeneity and Surface Chemistry in Polycrystalline Cathode Materials. Joule *2*, 464–477.

11. Gent, W.E., Li, Y., Ahn, S., Lim, J., Liu, Y., Wise, A.M., Gopal, C.B., Mueller, D.N., Davis, R., Weker, J.N., et al. (2016). Persistent State-of-Charge Heterogeneity in Relaxed, Partially Charged Li1−xNi3Co3Mn3O2 Secondary Particles. Adv. Mater. *28*, 6631–6638.

12. Fang, S., Yan, M., and Hamers, R.J. (2017). Cell design and image analysis for in situ Raman mapping of inhomogeneous state-of-charge profiles in lithium-ion batteries. J. Power Sources *352*, 18–25.

13. Nakamura, T., Watanabe, T., Kimura, Y., Amezawa, K., Nitta, K., Tanida, H., Ohara, K., Uchimoto, Y., and Ogumi, Z. (2017). Visualization of Inhomogeneous Reaction Distribution in the Model LiCoO2 Composite Electrode of Lithium Ion Batteries. J. Phys. Chem. C *121*, 2118–2124.

14. Nanda, J., Remillard, J., O'Neill, A., Bernardi, D., Ro, T., Nietering, K.E., Go, J.Y., and Miller, T.J. (2011). Local state-of-charge mapping of lithium-ion battery electrodes. Adv. Funct. Mater. *21*, 3282–3290.

15. Yang, Y., Xu, R., Zhang, K., Lee, S.-J., Mu, L., Liu, P., Waters, C.K., Spence, S., Xu, Z., Wei, C., et al. (2019). Quantification of Heterogeneous Degradation in Li-Ion Batteries. Adv. Energy Mater. *9*, 1900674.

16. Park, J., Zhao, H., Kang, S.D., Lim, K., Chen, C.C., Yu, Y.S., Braatz, R.D., Shapiro, D.A., Hong, J., Toney, M.F., et al. (2021). Fictitious phase separation in Li layered oxides driven by electro-autocatalysis. Nat. Mater. *20*, 991–999.

17. Rivera-Barrera, J.P., Muñoz-Galeano, N., and Sarmiento-Maldonado, H.O. (2017). Soc estimation for lithium-ion batteries: Review and future challenges.

18. Tran, M.K., and Fowler, M. (2020). A review of lithium-ion battery fault diagnostic algorithms: Current progress and future challenges. Algorithms *13*.

19. Hannan, M.A., Lipu, M.S.H., Hussain, A., and Mohamed, A. (2017). A review of lithium-ion battery state of charge estimation and management system in electric vehicle applications: Challenges and recommendations. Renew. Sustain. Energy Rev. *78*, 834–854.

20. Li, Y., El Gabaly, F., Ferguson, T.R., Smith, R.B., Bartelt, N.C., Sugar, J.D., Fenton, K.R., Cogswell, D.A., Kilcoyne, A.L.D., Tyliszczak, T., et al. (2014). Current-induced transition from particle-by-particle to concurrent intercalation in phase-separating battery electrodes. Nat. Mater. *13*, 1149–1156.

21. Wang, J., Chen-Wiegart, Y.C.K., and Wang, J. (2014). In operando tracking phase transformation evolution of lithium iron phosphate with hard X-ray microscopy. Nat. Commun. *5*, 1–10.

22. Tian, C., Xu, Y., Nordlund, D., Lin, F., Liu, J., Sun, Z., Liu, Y., and Doeff, M. (2018). Charge Heterogeneity and Surface Chemistry in Polycrystalline Cathode Materials. Joule *2*, 464–477.

23. Finegan, D.P., Quinn, A., Wragg, D.S., Colclasure, A.M., Lu, X., Tan, C., Heenan, T.M.M., Jervis, R., Brett, D.J.L., Das, S., et al. (2020). Spatial dynamics of lithiation and lithium plating during high-rate operation of graphite electrodes. Energy Environ. Sci. *13*, 2570–2584.

24. Finegan, D.P., Vamvakeros, A., Tan, C., Heenan, T.M.M., Daemi, S.R., Seitzman, N., Di Michiel, M., Jacques, S., Beale, A.M., Brett, D.J.L., et al. (2020). Spatial quantification of dynamic inter and intra particle crystallographic heterogeneities within lithium ion electrodes. Nat. Commun. *11*, 1–11.

25. Thomas-alyea, K.E., Jung, C., Smith, R.B., and Bazant, M.Z. (2017). In Situ Observation and Mathematical Modeling of Lithium Distribution within Graphite. *164*.

26. Qi, Y., and Harris, S.J. (2010). In situ observation of strains during lithiation of a graphite electrode. J. Electrochem. Soc. *157*, 741–747.

27. Merryweather, A.J., Schnedermann, C., Jacquet, Q., Grey, C.P., and Rao, A. (2021). Operando

optical tracking of single-particle ion dynamics in batteries. Nature *594*, 522–528.

28. Agrawal, S., and Bai, P. (2021). Operando Electrochemical Kinetics in Particulate Porous Electrodes by Quantifying the Mesoscale Spatiotemporal Heterogeneities. Adv. Energy Mater. *203344*, 1–12.

29. Wang, D.Y., Wei, C.Y., Lin, M.C., Pan, C.J., Chou, H.L., Chen, H.A., Gong, M., Wu, Y., Yuan, C., Angell, M., et al. (2017). Advanced rechargeable aluminium ion battery with a high-quality natural graphite cathode. Nat. Commun. *8*, 1–7.

30. Kravchyk, K. V., and Kovalenko, M. V. (2019). Rechargeable Dual-Ion Batteries with Graphite as a Cathode Key Challenges and Opportunities. Adv. Energy Mater. *9*.

31. Zhang, X., Tang, Y., Zhang, F., and Lee, C.S. (2016). A Novel Aluminum–Graphite Dual-Ion Battery. Adv. Energy Mater. *6*, 1–6.

32. Zhang, M., Song, X., Ou, X., and Tang, Y. (2019). Rechargeable batteries based on anion intercalation graphite cathodes. Energy Storage Mater. *16*, 65–84.

33. Smith, R.B., Khoo, E., and Bazant, M.Z. (2017). Intercalation kinetics in multiphase layered materials. 1–28.

34. Ohzuku, T. (1993). Formation of Lithium-Graphite Intercalation Compounds in Nonaqueous Electrolytes and Their Application as a Negative Electrode for a Lithium Ion (Shuttlecock) Cell. J. Electrochem. Soc. *140*, 2490.

35. Levi, M.D., Levi, E.A., and Aurbach, D. (1997). The mechanism of lithium intercalation in graphite film electrodes in aprotic media. Part 2. Potentiostatic intermittent titration and in situ XRD studies of the solid-state ionic diffusion. J. Electroanal. Chem. *421*, 89–97.

36. Thomas-alyea, K.E., Jung, C., Smith, R.B., and Bazant, M.Z. (2017). In Situ Observation and Mathematical Modeling of Lithium Distribution within Graphite. *164*, E3063.

37. Bai, P., Cogswell, D.A., and Bazant, M.Z. (2011). Suppression of phase separation in LiFePO4 nanoparticles during battery discharge. Nano Lett. *11*, 4890–4896.

38. Guo, Y., Smith, R.B., Zhonghua, Y., Efetov, D.K., Wang, J., Kim, P., Bazant, M.Z., and Brus, L.E. (2016). Li Intercalation into Graphite: Direct Optical Imaging and Cahn−Hilliard Reaction Dynamics. J. Phys. Chem. Lett. *7*, 2151–2156.

39. Li, Y., Chen, H., Lim, K., Deng, H.D., Lim, J., Fraggedakis, D., Attia, P.M., Lee, S.C., Jin, N., Moškon, J., et al. (2018). Fluid-enhanced surface diffusion controls intraparticle phase transformations. Nat. Mater. *17*, 915–922.

40. Cogswell, D.A., and Bazant, M.Z. (2013). Theory of coherent nucleation in phase-separating nanoparticles. Nano Lett. *13*, 3036–3041.

41. Bai, P., and Tian, G. (2013). Statistical kinetics of phase-transforming nanoparticles in LiFePO 4 porous electrodes. Electrochim. Acta *89*, 644–651.

42. Kondo, H., Sasaki, T., Barai, P., and Srinivasan, V. (2018). Comprehensive Study of the Polarization Behavior of LiFePO 4 Electrodes Based on a Many-Particle Model. *165*, A2047.

43. Dreyer, W., Jamnik, J., Guhlke, C., Huth, R., Moškon, J., and Gaberšček, M. (2010). The thermodynamic origin of hysteresis in insertion batteries. Nat. Mater. *9*, 448–453.

44. Lim, J., Li, Y., Alsem, D.H., So, H., Lee, S.C., Bai, P., Cogswell, D.A., Liu, X., Jin, N., Yu, Y.S., et al. (2016). Origin and hysteresis of lithium compositional spatiodynamics within battery primary particles. Science (80-. ). *353*, 566–571.

45. Tang, M., Carter, W.C., and Chiang, Y.M. (2010). Electrochemically driven phase transitions in insertion electrodes for lithium-ion batteries: Examples in lithium metal phosphate olivines.

46. Bazant, M.Z. (2013). Theory of chemical kinetics and charge transfer based on nonequilibrium thermodynamics. Acc. Chem. Res. *46*, 1144–1160.

47. Dresselhaus, M.S., and Dresselhaus, G. (2002). Intercalation compounds of graphite. Adv. Phys. *51*, 1–186.

48. Song, X.Y., Kinoshita, K., and Tran, T.D. (1996). Microstructural Characterization of Lithiated Graphite. J. Electrochem. Soc. *143*, L120–L123.

49. Ferguson, T.R., and Bazant, M.Z. (2014). Phase transformation dynamics in porous battery electrodes. Electrochim. Acta *146*, 89–97.

50. Cogswell, D.A., and Bazant, M.Z. (2012). Coherency strain and the kinetics of phase separation in LiFePO 4 nanoparticles. ACS Nano *6*, 2215–2225.

51. Ferguson, T.R., and Bazant, M.Z. (2012). Nonequilibrium thermodynamics of porous electrodes. J. Electrochem. Soc. *159*.

52. Newman, J., and Thomas-alyea, K.E. (2004). Electrochemical Systems (John Wiley & Sons, Inc., New York, NY).

53. Srinivasan, V., and Newman, J. (2004). Discharge model for the lithium iron-phosphate electrode. J. Electrochem. Soc. *151*.

54. Ferguson, T.R., and Bazant, M.Z. (2014). Phase transformation dynamics in porous battery electrodes. Electrochim. Acta *146*, 89–97.

55. Mori, F., Kubouchi, M., and Arao, Y. (2018). Effect of graphite structures on the productivity and quality of few-layer graphene in liquid-phase exfoliation. J. Mater. Sci. *53*, 12807–12815.

56. Wang, F., Graetz, J., Moreno, M.S., Ma, C., Wu, L., Volkov, V., and Zhu, Y. (2011). Chemical distribution and bonding of lithium in intercalated graphite: Identification with optimized electron energy loss spectroscopy. ACS Nano *5*, 1190–1197.

57. Fraggedakis, D., Nadkarni, N., Gao, T., Zhou, T., Zhang, Y., Han, Y., Stephens, R.M., Shao-Horn,

Y., and Bazant, M.Z. (2020). A scaling law to determine phase morphologies during ion intercalation. Energy Environ. Sci.

58. Tsai, P.C., Wen, B., Wolfman, M., Choe, M.J., Pan, M.S., Su, L., Thornton, K., Cabana, J., and Chiang, Y.M. (2018). Single-particle measurements of electrochemical kinetics in NMC and NCA cathodes for Li-ion batteries. Energy Environ. Sci. *11*, 860–871.

59. Li, J., Xiao, X., Yang, F., Verbrugge, M.W., and Cheng, Y.T. (2012). Potentiostatic intermittent titration technique for electrodes governed by diffusion and interfacial reaction. J. Phys. Chem. C *116*, 1472–1478.

60. Bazant, M.Z. (2017). Thermodynamic stability of driven open systems and control of phase separation by electro-autocatalysis. Faraday Discuss. *199*, 423–463.